A model-based framework to prevent excavator induced damage in operations on natural gas pipelines

Engineering Failure Analysis 164 (2024) 108659

Contents lists available at ScienceDirect

Engineering Failure Analysis

journal homepage: www.elsevier.com/locate/engfailanal

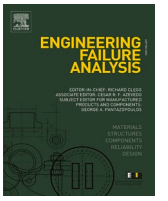

A model-based framework to prevent excavator induced damage in operations on natural gas pipelines

Matteo Melchiorre [a,*], Luca Bacchi [b], Pierpaolo Palmieri [a], Andrea Ruggeri [a], Laura Salamina [a], Stefano Mauro [a]

[a] Department of Mechanical and Aerospace Engineering, Politecnico di Torino, 10129, Torino, Italy
[b] SNAM Rete Gas, 20097, San Donato Milanese, Milano, Italy

ARTICLE INFO

Keywords:
Gas pipeline
Excavator
Digging force
Dent
Model-based analysis

ABSTRACT

Despite the presence of numerous safety precautions, the primary cause of damage to underground pipes is often attributed to external interference from excavators during their operations. To address this issue, this paper introduces a model-based approach that incorporates both static and dynamic contact in assessing the damage caused by excavators on pipes. The objective of this method is to offer a practical tool that can assist in determining the appropriate excavator size for buried gas pipes. By identifying the maximum safe excavator size, the aim is to minimize the potential risks of mechanical damage to the pipe, to prevent hazards for operators and to protect the integrity of the pipeline. For this purpose, a comprehensive excavator model is constructed. Following this, a suitable damage model for the pipe is selected and the interaction between the bucket tooth and the pipe is modelled. To enhance accuracy, the excavator and pipe are interconnected through the solution of damped contact equations, which take into account the stiffnesses of both the pipe and excavator, as well as the damping effect resulting from pipe deformation. Results provide valuable insight into the potential damage caused to the pipe, which can be attributed to either static or dynamic contacts, depending on which excavator is being used. Failure is addressed by plastic dent, that can be avoided by selecting the most suitable excavator size. Moreover, the analysis of dent depth caused by various excavators on different pipes for gas transmission, opens to the possibility of mitigating the risk of failures by limiting the excavator workspace.

1. Introduction

Natural gas is one of the most important energy sources for industry, power generation and domestic uses. To efficiently supply large quantities of natural gas to consumers, pipeline transport offers a widely adopted and cost-effective solution; for instance, the extension of gas pipelines network in Europe in 2019 was over 140 000 km, as reported in [1]. Given the importance of natural gas as energy source, its delivery must be as reliable and continuous as possible, therefore failures of the pipeline should be avoided. To achieve this, agencies worldwide, like the European Gas Pipeline Incident Data Group (EGIG) [1] and the Pipeline and Hazardous Materials Safety Administration (PHMSA) [2], collect data on pipeline damages and failures. During last 50 years in EGIG database

* Corresponding author.
E-mail addresses: matteo.melchiorre@polito.it (M. Melchiorre), luca.bacchi@snam.it (L. Bacchi), pierpaolo.palmieri@polito.it (P. Palmieri), andrea.ruggeri@polito.it (A. Ruggeri), laura.salamina@polito.it (L. Salamina), stefano.mauro@polito.it (S. Mauro).

https://doi.org/10.1016/j.engfailanal.2024.108659
Received 9 February 2024; Received in revised form 25 June 2024; Accepted 9 July 2024
Available online 14 July 2024

were recorded 1411 incidents, 45 of which happened in 2017–2018 [1].

In general, an incident can cause both a failure and a damage of the pipeline: failures can make the network unavailable for a period or cause casualties; damaging generally does not involve unavailability of the network, however it could worsen in time resulting in a delayed failure. Therefore, attention must be paid on preventing both failures and damages of the pipes.

For example, the threat of mechanical damage due to external interference with excavators is normally managed by the transmission pipeline operators with proper relationships and communications with all the potential stakeholders in order to avoid third parties damaging and with prevention measures, like mechanical protections of pipelines and specific and dedicated procedures for works close to the operating pipelines. Such procedures normally include the preventive pipeline axis positioning, the proper choice of the kind and sizes of excavators and the rules for excavating (always including manual digging when close to the pipeline). However, these safety procedures are for the most part operator-dependent, so incorrect application can lead to errors. For instance, EGIG reports that external interference from excavators' operations is the most frequent cause of underground pipe damage and failure [1]. Moreover, PHMSA data show that the excavation damage for onshore gas transmission and distribution pipelines in U.S. is the primary cause of significant incidents until 2008 [2].

Localized mechanical damage from digging activities occurs when the tooth of a bucket gets in contact with the pipe with a non-zero force. This contact can lead to various types of damage, including geometry modifications (dent and gouges, see Fig. 1), residual stress (from denting and re-rounding), and metallurgical variation (thermal cycling due to friction and local hardening), [2,3]. The mechanical damage of buried pipelines can be gouge, dent or a combination of both [3], while a mechanical failure involves puncture or rupture of the pipe due to excavation (Fig. 2). A dent is a concave deformation of the pipe cross-section, which produce a disturbance on the curvature of the pipe wall without a section reduction, resulting from plastic deformation due to the contact with an external object as an excavator bucket. Dent size is usually measured through dent depth, which is the maximum distance between damaged and undamaged point of a cross section of the pipe [4]. Dents can reduce the burst pressure and fatigue life of pipes; on the other hand, it was shown that dents at welds can significantly reduce fatigue life either for ductile pipes [5]. On the other hand, a gouge is a surface defect of a pipeline caused by the removal of wall material after the contact with an external object drawn across the surface. Gouges provide both mechanical damages, acting as stress concentrator, and metallurgical damages: the material undergoes strain hardening and thermal heating due to friction forces, hence at gouges the microstructure turns different from undamaged material. The above mentioned damages can lead to failures as leak or rupture, resulting in gas ejection [6].

Whenever a pipe experiences an incident during excavation operations, even if without incur immediate failing (puncture), the damage can further progress into a failure in particular operating and environmental conditions, thus resulting in a delayed failure. Therefore, the assessment of damage features is important for pipeline safety and integrity management [2]. Due to the importance of reliable assessment criteria, fifteen international oil and gas companies joined to develop the Pipeline Defect Assessment Manual (PDAM), in which best practices for assessment of pipeline defects are documented to help engineers and technicians to make decisions and maintain an high level of safety [7]: in particular, methods are given to assess the burst and fatigue strength of a defect with certain characteristics when subjected respectively to static and dynamic loading. Either European Pipeline Research Group (EPRG) has developed rules and best-practices to assess external damages, such as the critical defect dimensions, fatigue life of defects and prevention of external damage [3]. These rules deal with the relationship between damage size and pressure resistance. For example, in EPRG reports [3] "role of thumb" criteria are to predict resistance of a pipe to dent, gouge and their combination.

Efforts were also made in past years to develop analogue relations between applied load and damage magnitude, and between excavator size and applied load. Coupling the relation between excavator mass and maximum applied force, between load and dent depth and finally between depth and burst pressure, one could manage a quantitative risk assessment for a pipeline when digging operations with excavators have to be performed close to the pipeline itself.

Several experimental campaigns have been undertaken to validate analytic and finite element models of pipelines subjected to excavator tooth load, as listed below [8]. Full-scale test of excavators impacting on pipelines were made in'90 by EPRG to evaluate digging incidents in both static and dynamic conditions [3]. In EPRG reports the damage capacity of excavators from 7.8 to 65.5 ton of size was estimated obtaining general relations between excavator mass, tooth size, static force (either bucket or stick) and

Fig. 1. Pipe portion with dents (marked with letters A, C, D), gauges (E, F, G), and combination of both (B).

Fig. 2. Typical excavator puncture on pipe surface.

amplification factors.

Apart from experimental investigations, which are expensive and time-consuming, efforts were made to develop analytical and numerical models to predict the relations among external load, operating conditions, dent size and failure pressure of pipelines. In [9] authors developed an analytical quasi-static model of the pipe to predict the relationship between applied force and dent depth. Gresnigt and Karamanos investigated the response of internally pressurized pipe subject to lateral quasi-static load through experiments, FEM and an analytical shell model of the pipe [10,11]. They assumed the total load response consisting of three parts (elastic, plastic, and membrane) to develop the analytic model; the role of denting tool orientation, size and internal pressure on the elasto-plastic response were examined in comparison with test data. Brooker [12] developed a two phase analytic model based on shell theory for the elastic and finite-deflection limit for the plastic response of a pressurized pipeline under lateral denting of a rectangular excavator tooth, and then compared it with FE and experimental results. In [13] authors studied the quasi-static response of flexibly supported pressurized pipes to lateral impacts, thus taking in account the bed compliance. Dou et al. [14] used numerical methods to establish an analytical model to investigate the influence of some parameters on pressurized pipelines response to lateral loading.

More recent studies, taking advantage of the development in computing power in recent years, are moving towards finite element simulations. Brooker [15] studied the puncture behaviour of buried pipelines under excavator tooth loading through an accurate definition of material damage and ductile failure mechanisms, comparing results with experiments; in [16] the validated model was used for a parametric study on tool size and shape, internal pressure, pipe diameter and thickness, material grade. Hyde et al. [17] validated a shell-based FE model on experimental data of puncture load of pressurized pipes at various pressures; the numerical model has shown good agreement with test data, although at higher pressures the simulated resistance was higher. Han et al. [18] studied the effects of diameter-to-thickness ratio and indenter displacement with a FE model, considering pipe response in terms of puncture load, plastic deformations and rebound ratio. All of these models take in account the maximum static load applied on a pipe, thus ignoring the dynamic effects on the pipe and the excavator. Xu et al. [19] developed a multi-body model of the excavator and the pipe to simulate the transient effects of the interaction, in particular the real maximum applied load due to dynamic effects of the excavator; experimental tests were conducted in both pseudo-static and dynamic conditions to estimate the real digging force of the excavator in real mining conditions.

Although norms exist to determine characteristic features of excavators, the maximum load in worst case scenario is not easy to determine, which corresponds to the condition of the bucket impacting on the pipe by concurring action of all cylinders, belonging to a not-working scenario. The BS-ISO 6015:2006 [20] defines typical loads of interest and the manner to measure them, but no reference is made about the maximum worst case load of interest. A dynamic model of the excavator is thus necessary to determine the applied load at tooth tip in a given configuration in order to find the worst scenario force. In'90 the interest on automatization of digging operations held researchers to develop kinematic and dynamic models to relate motion of actuators and the tool [21,22,23]. In [21] and [23] authors evidenced similarities between excavators and a robotic arm with four links and four joints, thus allowing to apply existing methods for robotics modelling to obtain the excavator dynamic model. In [24] authors coupled the mechanical model of excavator with hydraulic model of cylinder to understand the coupling issues for trajectory planning. More recently dynamic models of excavators and hydraulic actuators were employed to study the dynamic stability issues during normal operations ([25,26]) and during non-normal but widespread lifting use of excavator ([27]). Lagrangian method was used to develop the dynamic model in [28] to investigate vibration loads during normal digging operations.

The ERPG tests allowed to determine an empirical relation between excavator size (in tons) and the maximum load it can exert on a pipe in worst case scenario [3], which are only applicable on excavators which size falling in the experimental range; furthermore, technology improvements in past years can have led to a significant difference between tested excavators and those of later design. Hence the need of a simulation tool which can predict the maximum damage depth of a pipe of certain dimensions in the worst-case scenario starting from the construction features of the excavator.

The state of the art has shown that there are studies aimed at analysing and quantifying the damage to pipes due to interaction with

excavators, but, to the authors knowledge, the literature lacks a tool that is at the same time: comprehensive, i.e. that allows the worst-case damage to be assessed, taking into account all the possible operating conditions of the excavation; efficient, i.e. that is not based on experimental tests, that can be costly and time-consuming; and parametric, i.e. that can easily adapt to the different characteristics of the pipes and excavators. To address all these aspects, this paper presents a model-based method for assessing potential pipe damage by excavators, that takes into account static and dynamic contacts. The method aims to provide a practical tool that can prevent failure by identifying the maximum safe excavator size for a task in which a given pipe is involved, in order to minimize the risk of puncture or damage of the operating pipeline.

Specifically, relying on models, the method presented in this paper uses equations to calculate the digging force or energy at impact with the pipe, and to estimate the dent on the pipe resulting from accidental bucket-pipe contact. To do so, a damage model for the pipe is chosen, an excavator model is developed and a model of the interaction between tooth and pipe is proposed. Excavator and pipe models can be found in the literature. However, in this work they are revised and simplified for an easier application on buried gas pipes. On the other hand, the interaction model for calculation of pipe damage depth is novel, and takes into account stiffnesses of pipe and excavator, as well as damping effect due to deformation of the pipe.

The main contributions of this work to the state of the art can be summarized in the following points:

- A numerical scheme for calculation of maximum digging force and maximum kinetic energy of an excavator, that considers limit conditions, i.e. the maximum hydraulic circuit pressure and tipping, and that focuses on the configurations that are relevant for buried pipes application.
- An excavator-pipe interaction model, that involves stiffness and damping effects, and that allows to calculate denting displacement on the pipe for static and dynamic contacts.
- A method to analyze simulation results for the selection of the excavator on the basis of dent curves.
- A novel preventive action that considers the possibility to limit the excavator workspace in order to mitigate the risk of failure.

The following chapter provides a more detailed overview of the work, introducing the tools used, describing how they are presented in the article, and how they are combined within the model-based framework.

2. Methods

The method is based on a theoretical and very severe approach that tries to estimate the effects of accidental contact between the excavator and the pipe in the worst case, without considering all the preventions measures (out of the scope of this paper) that would normally avoid the possibility of the damage itself. These contact effects are estimated by calculating the penetration of the bucket tooth into the pipe in the worst possible case. Once the penetration has been calculated, it is assessed whether it exceeds the plastic limit, thus resulting in a dent.

Since we will see that the dent depends on both the excavator and the pipe, an analysis can be carried out as the size of the excavator and the pipe itself changes, in order to be able to say whether an excavator is suitable for operating close to a certain pipe or, on the contrary, there is a risk of damage.

The damage is calculated by coupling excavator and the pipe mathematical models through a contact model, which is constructed on the basis of the analytical relationship between the force imparted by the excavator tooth and the dent in the pipe.. In particular, field experience suggests that the analysis should focus on two possible mode of contact that may occur during a digging operation:

i) Static contact: the pipe is buried and the operator places the bucket teeth on the part of the ground to be removed, then rotates the bucket and while digging encounters a pipe; in this case the excavator applies the digging force at low velocities, thus the prevalent effect on the pipe is the hydraulic static force, and the kinetic energy contributions are negligible.
ii) Dynamic contact: the pipe has already been uncovered, and the operator performs a wrong manoeuvre, so the tooth/bucket of the excavator impacts on the pipe at high speed; there the kinetic energy effects must be taken in account.

For the sake of finding the worst-case condition, both scenarios must be considered, thus static and dynamic model of the collision are required.

The basis for static contact is the calculation of the maximum static force that can be exerted by the excavator. For dynamic contact, on the other hand, it is necessary to consider the excavator's initial conditions at the moment of impact, so the excavator's maximum kinetic energy must be calculated. These aspects are dealt with in Chapter 3, which provides a complete modelling of the excavator and examples of calculating the maximum static force and kinetic energy of an excavator.

Next, in order to be able to assess the damage, the pipe model will be introduced in Chapter 4, which is based on the Gresnight equations.

In Chapter 5, the contact model is introduced and the logic by which the excavator and pipe model are coupled is described. It is anticipated that the contact model considers an equilibrium relation that takes into account inertia, stiffness and damping effects, as well as initial condition. In particular, by changing the initial conditions of the problem, it will be possible to discriminate between static and dynamic contact cases. For example, in static contact the initial speed of the excavator is zero, while in dynamic contact it is derived from the calculation of maximum kinetic energy.

Finally, results are presented in Chapter 6 in terms of denting displacement, i.e. the penetration of the bucket tooth into the pipe, for both the static and the dynamic case. The analysis of the results will be done by means of dent charts, i.e. charts linking the dent to the

characteristics of the excavator considered or the pipe geometry. Moreover, dent charts can be used to identify the risk related to scenarios with different probability of occurrence. In particular, two different situations will be distinguished: the first is the worst possible case, with a low probability of occurrence; the second one is related to an operative and more probable condition. The detailed description of these cases is anticipated at the end of Chapter 3. This approach allows to relate the size of an excavator to something bound to the risk level associated with its employment.

3. Excavator model

The excavator is modelled as a three-link planar arm connected by means of revolute joints and moved by linear actuators (Fig. 3). Let xyz denote the axis of the base frame. The pose of link $i = 1, 2, 3$ is described by position and orientation of the frame $x_i y_i z_i$. The fixed length a_i represents the distance between two consecutive frames, while θ_i indicate the angle between axes x_{i-1} and x_i.

To define the configuration of the excavator, the generalized coordinates θ_i can be gathered in the vector of joint variables $\boldsymbol{q} = [\theta_1 \theta_2 \theta_3]^T$. The pose of the end-effector, i.e. point D placed at the bucket teeth, with respect to the base frame can be expressed in terms of position $\boldsymbol{p}_D$ and orientation, the latter identified by the angle ϕ between axes x and x_3.

The parameter γ is the angle identified by x_3 and the direction of the bucket teeth, and depends only on the type of bucket. The length d is the distance between the origin of the base frame and the ground.

In the following sections the kinematic analysis, as well as the kinetic energy and static force analysis are carried out for the study of the maximum force exerted on the pipe in the case of dynamic or static contact.

3.1. Kinematic analysis

The kinetic energy formulation requires the rotational velocities of the links, as well as their translational velocity at the center of mass. For this, the kinematic analysis of the excavator is carried out. The analysis is divided in two parts.

The first part provides the relationships between the linear velocity of the actuators and the joint velocities $\dot{\theta}_i$. Thus, one can calculate joint velocities corresponding to the maximum rated speed of the actuators. In this part, some important geometric expressions that will also be useful for the static force analysis are obtained. In this part, equations are obtained from the analysis of the mechanism that synthesizes the kinematics of the excavator.

As these expressions depend on the configuration of the excavator, in the second part the problem of direct kinematic is addressed. Furthermore, inverse kinematics is considered in order to find the angles θ_1, θ_2 and θ_3 that correspond to given digging position and orientation, the latter being more representative in practice. Equations of this part are derived from the kinematic analysis on the 3-link planar arm in [29].

3.1.1. Formulation of joint velocities

The formulation is divided into 3 subsystems. In the first one, the boom is studied; the second subsystem is made of the arm; the analysis moves on the third subsystem, intended as the four-bar mechanism that activate the bucket.

- Boom mechanism

A schematic representation of the subsystem related to the boom is given in Fig. 4. Let l_{AG} denote the distance between joints A-G (this notation is assumed hereafter, to indicate distances between joints). Lengths l_{AG}, l_{AH} and l_{BH} are fixed; l_{GH} is the length of the boom cylinder and depends on the configuration of the excavator. Moreover, ε_1 is the given angle between the horizontal and the segment

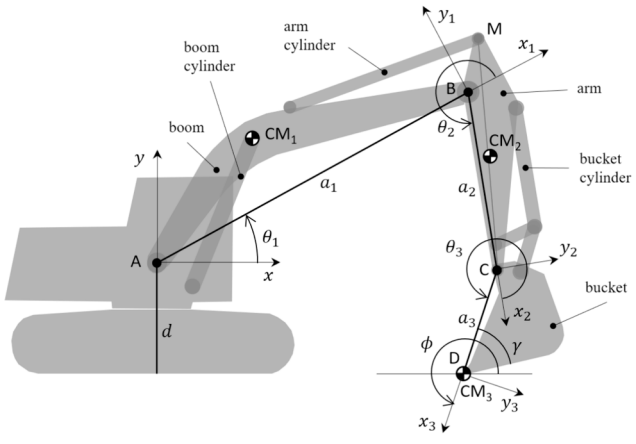

Fig. 3. Scheme of the excavator as a three link planar arm.

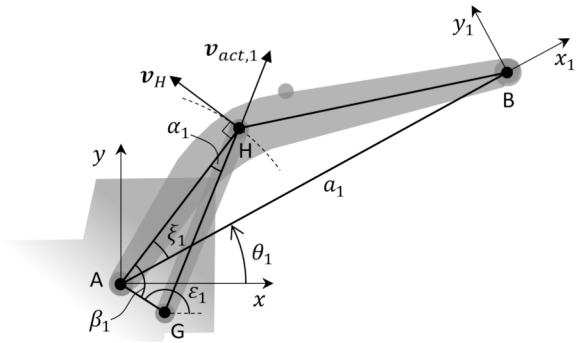

Fig. 4. Scheme of the boom.

$\overline{AG}$.

By Carnot's theorem:

$$\alpha_1 = \cos^{-1}\left(\frac{l_{GH}^2 + l_{AH}^2 - l_{AG}^2}{2l_{GH}l_{AH}}\right) \tag{1}$$

Let $\boldsymbol{v}_{act,1}$ denote the boom cylinder rod velocity. Joint H rotates about A so its velocity $\boldsymbol{v}_H$ must be perpendicular to segment $\overline{AH}$. Moreover, the rotational velocity $\dot{\beta}_1$ is equal to $\dot{\theta}_1$ because $\overline{AH}$ is rigid with respect to $\overline{AB}$. The following equation holds:

$$\dot{\theta_1} = \dot{\beta_1} = \frac{|\boldsymbol{v}_H|}{l_{AH}} = \frac{|\boldsymbol{v}_{act,1}|}{l_{AH}\sin\alpha_1} \tag{2}$$

On the other hand, the angle θ_1 can be written as:

$$\theta_1 = \varepsilon_1 + \beta_1 - \xi_1 - \pi \tag{3}$$

where ξ_1 can be computed as:

$$\xi_1 = \cos^{-1}\left(\frac{a_1^2 + l_{AH}^2 - l_{BH}^2}{2a_1 l_{AH}}\right) \tag{4}$$

- Arm mechanism

A schematic representation of arm mechanism is given in Fig. 5. Lengths l_{BL}, l_{BM} and l_{AL} are fixed; l_{LM} is the length of the arm cylinder and depends on the configuration.

By Carnot's theorem applied to the triangle *BLM*, the rotational velocity $\dot{\theta}_2$ can be computed as:

$$\alpha_2 = \cos^{-1}\left(\frac{l_{LM}^2 + l_{BM}^2 - l_{BL}^2}{2l_{LM}l_{BM}}\right) \tag{5}$$

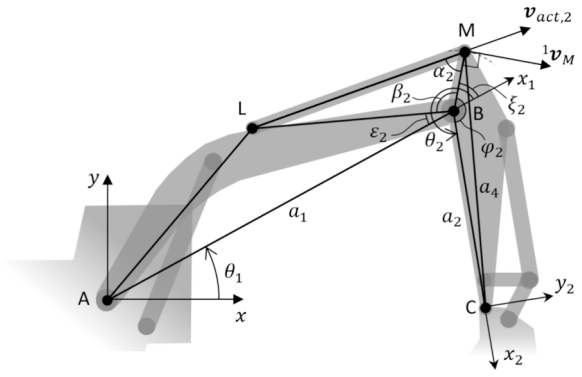

Fig. 5. Scheme of the arm.

$$\dot{\theta}_2 = \frac{|{}^1\boldsymbol{v}_M|}{l_{BM}} = \frac{|\boldsymbol{v}_{act,2}|}{l_{BM}\sin\alpha_2} \tag{6}$$

where $\boldsymbol{v}_{act,2}$ denotes the arm cylinder rod velocity, while ${}^1\boldsymbol{v}_M$ is the velocity of joint M observed in the boom frame x_1y_1.

From Fig. 6, the angle θ_2 can be written as:

$$\theta_2 = 2\pi - \varphi_2 + \xi_2 \tag{7}$$

where φ_2 is given by:

$$\varphi_2 = \cos^{-1}\left(\frac{a_2^2 + l_{BM}^2 - a_4^2}{2a_2 l_{BM}}\right) \tag{8}$$

while ξ_2 is defined introducing β_2 and ε_2:

$$\varepsilon_2 = \cos^{-1}\left(\frac{l_{BL}^2 + a_1^2 - l_{AL}^2}{2l_{BL}a_1}\right) \tag{9}$$

$$\beta_2 = \cos^{-1}\left(\frac{l_{BL}^2 + l_{BM}^2 - l_{LM}^2}{2l_{BL}l_{BM}}\right) \tag{10}$$

$$\xi_2 = \pi - \varepsilon_2 - \beta_2 \tag{11}$$

- Bucket mechanism

The third actuator moves the input link of the four-bar linkage that activates the bucket. Lengths l_{NS}, l_{NQ}, l_{MN} and l_{MS} are fixed. The variable l_{QS} denotes the length of the bucket actuator. By observing Fig. 6, one can find the rotational velocity $\dot{\xi}_3$ of the input link as:

$$\alpha_3 = \cos^{-1}\left(\frac{l_{QS}^2 + l_{NQ}^2 - l_{NS}^2}{2l_{QS}l_{NQ}}\right) \tag{12}$$

$$\dot{\xi}_3 = \frac{|{}^2\boldsymbol{v}_Q|}{l_{NQ}} = -\frac{|\boldsymbol{v}_{act,3}|}{l_{NQ}\sin\alpha_3} \tag{13}$$

where $\boldsymbol{v}_{act,3}$ is the bucket cylinder rod velocity and ${}^2\boldsymbol{v}_Q$ is the velocity of joint Q relative to the arm frame x_2y_2. Moreover, by assuming that joints N and C are aligned with M, the angle ξ_3 can be written as:

$$\xi_3 = \pi - \varepsilon_3 - \beta_3 \tag{14}$$

where ε_3 and β_3 are defined as:

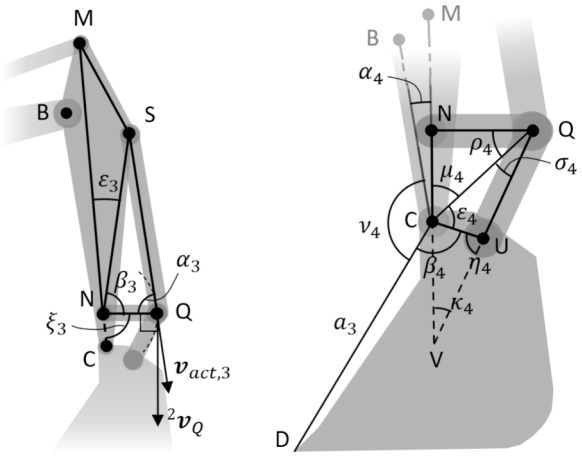

Fig. 6. Scheme of the bucket mechanism.

$$\varepsilon_3 = \cos^{-1}\left(\frac{l_{NS}^2 + l_{MN}^2 - l_{MS}^2}{2 l_{NS} l_{MN}}\right) \tag{15}$$

$$\beta_3 = \cos^{-1}\left(\frac{l_{NS}^2 + l_{NQ}^2 - l_{QS}^2}{2 l_{NS} l_{NQ}^2}\right) \tag{16}$$

To find the expressions of $\dot{\theta}_3$ and θ_3, the four-bar linkage mechanism is analyzed. By observing Fig. 6, lengths l_{CN}, l_{QU} and l_{CU} are fixed. Angles α_4 and β_4 are given and depend on the excavator model and on the bucket type.

The length of the diagonal l_{CQ} can be found as:

$$l_{CQ} = \sqrt{l_{CN}^2 + l_{NQ}^2 - 2 l_{CN} l_{NQ} \cos\xi_3} \tag{17}$$

Moreover, angles ε_4, μ_4 and ν_4 are introduced as:

$$\varepsilon_4 = \cos^{-1}\left(\frac{l_{CQ}^2 + l_{CU}^2 - l_{QU}^2}{2 l_{CQ} l_{CU}}\right) \tag{18}$$

$$\mu_4 = \cos^{-1}\left(\frac{l_{CQ}^2 + l_{CN}^2 - l_{NQ}^2}{2 l_{CQ} l_{CN}}\right) \tag{19}$$

$$\nu_4 = 2\pi - \alpha_4 - \beta_4 - \mu_4 - \varepsilon_4 \tag{20}$$

Thus, θ_3 is calculated as:

$$\theta_3 = \pi + \nu_4 \tag{21}$$

As regard the rotational velocity $\dot{\theta}_3$, by considering the instant center of rotation V, one can write:

$$\dot{\theta}_3 = \dot{\xi}_3\left(\frac{l_{CV} + l_{CN}}{l_{CV}}\right) \tag{22}$$

Length l_{CN} is given, while l_{CV} must be determined. By law of sines:

$$l_{CV} = l_{CU}\frac{\sin\eta_4}{\sin\kappa_4} \tag{23}$$

In (23), η_4 and κ_4 can be obtained by observing triangles CQU and CUV:

$$\eta_4 = \varepsilon_4 + \sigma_4 \tag{24}$$

$$\kappa_4 = \pi - \xi_3 - \sigma_4 - \rho_4 \tag{25}$$

where σ_4 and ρ_4 are given by:

$$\sigma_4 = \cos^{-1}\left(\frac{l_{CQ}^2 + l_{QU}^2 - l_{CU}^2}{2 l_{CQ} l_{QU}}\right) \tag{26}$$

$$\rho_4 = \pi - \xi_3 - \mu_4 \tag{27}$$

3.1.2. Direct and inverse kinematics

Starting from vector of joint variables $\boldsymbol{q}$, it is possible to obtain the pose of bucket teeth through direct kinematics. From [29], for the three-link planar arm, the transformation of link i with respect to link $i-1$ is given by the matrix ${}^{i-1}\boldsymbol{A}_i$ in the form:

$${}^{i-1}\boldsymbol{A}_i(\theta_i) = \begin{bmatrix} c_i & -s_i & 0 & a_i c_i \\ s_i & c_i & 0 & a_i s_i \\ 0 & 0 & 1 & 0 \\ 0 & 0 & 0 & 1 \end{bmatrix} \tag{28}$$

where the contracted form c_i and s_i indicate $\cos\theta_i$ and $\sin\theta_i$, respectively. Thus, the pose of the end-effector is obtained as:

$$\boldsymbol{A}_3 = \boldsymbol{A}_1\,{}^1\boldsymbol{A}_2\,{}^2\boldsymbol{A}_3 = \begin{bmatrix} c_{123} & -s_{123} & 0 & a_1 c_1 + a_2 c_{12} + a_3 c_{123} \\ s_{123} & c_{123} & 0 & a_1 s_1 + a_2 s_{12} + a_3 s_{123} \\ 0 & 0 & 1 & 0 \\ 0 & 0 & 0 & 1 \end{bmatrix} \tag{29}$$

where the contracted form c_{12}, c_{123}, s_{12}, s_{123} indicate $\cos(\theta_1+\theta_2)$, $\cos(\theta_1+\theta_2+\theta_3)$, $\sin(\theta_1+\theta_2)$ and $\sin(\theta_1+\theta_2+\theta_3)$, respectively.

In practice, it is convenient to express the digging configuration in terms of position and orientation of the teeth of the bucket. Because the digging force depends on the configuration of the excavator, it is useful to compute joint angles starting from the bucket pose. This translates into the inverse kinematics problem.

For a three-link planar arm, given the coordinates of the digging point p_{Dx}, p_{Dy} and the angle ϕ, the following system holds:

$$\begin{cases} \phi = \theta_1 + \theta_2 + \theta_3 \\ p_{Cx} = p_{Dx} - a_3 c_\phi = a_1 c_1 + a_2 c_{12} \\ p_{Cy} = p_{Dy} - a_3 s_\phi = a_1 s_1 + a_2 s_{12} \end{cases} \tag{30}$$

where p_{Cx} and p_{Cy} denote the coordinates of point C in the base frame. Squaring and summing the last two equations of (30), it is possible to solve for c_2 and s_2:

$$\begin{cases} c_2 = \dfrac{p_{Cx}^2 + p_{Cy}^2 - a_1^2 - a_2^2}{2a_1 a_2} \\ s_2 = \pm\sqrt{1 - c_2^2} \end{cases} \tag{31}$$

thus, the angle θ_2 is given by:

$$\theta_2 = \text{Atan2}(s_2, c_2) \tag{32}$$

notice that in (31) the relevant solution for the excavator is the one corresponding to the negative sign of s_2, which identifies the elbow-up posture of the three-link planar arm.

By substituting (32) in (30), one has:

$$\begin{cases} s_1 = \dfrac{(a_1 + a_2 c_2) p_{Cy} - a_2 s_2 p_{Cx}}{p_{Cx}^2 + p_{Cy}^2} \\ c_1 = \dfrac{(a_1 + a_2 c_2) p_{Cx} + a_2 s_2 p_{Cy}}{p_{Cx}^2 + p_{Cy}^2} \end{cases} \tag{33}$$

which gives θ_1 as:

$$\theta_1 = \text{Atan2}(s_1, c_1) \tag{34}$$

Finally, it is straightforward to obtain θ_3 from the first equation of (25):

$$\theta_3 = \phi - \theta_1 - \theta_2 \tag{35}$$

3.2. Kinetic energy analysis

Let m_i denote the mass of link i. Let $\boldsymbol{I}_i$ denote the inertia tensor relative to the center of mass of link i when expressed in the base frame. From [29], the kinetic energy of the excavator $\mathscr{T}$ under the action of the three actuators is given by the sum of the contributions relative to the motion of each link:

$$\mathscr{T} = \sum_{i=1}^{3} \left(\frac{1}{2} m_i \boldsymbol{v}_{CMi}^T \boldsymbol{v}_{CMi} + \frac{1}{2} \boldsymbol{\omega}_i^T \boldsymbol{I}_i \boldsymbol{\omega}_i \right) \tag{36}$$

where $\boldsymbol{v}_{CMi}$ is the velocity of the center of mass of link i and $\boldsymbol{\omega}_i$ is the angular velocity of link i, both referred to the base frame.

The first term in (36) represents the translational part of the kinetic energy. Velocities $\boldsymbol{v}_{CMi}$ depend on the configuration $\boldsymbol{q}$ and on the vector of joint velocities $\dot{\boldsymbol{q}} = \begin{bmatrix} \dot{\theta}_1 \dot{\theta}_2 \dot{\theta}_3 \end{bmatrix}^T$. They can be obtained as:

$$\boldsymbol{v}_{CM_i} = \mathscr{J}_{\boldsymbol{v}_{CMi}} \dot{\boldsymbol{q}} \tag{37}$$

where $\mathscr{J}_{\boldsymbol{v}_{CMi}}$ is the partial Jacobian, i.e. the part of the Jacobian computed at the center of mass CM_i which contributes to the linear velocity only. For the three-link planar arm in Fig. 4, one has:

$$\begin{aligned} \mathscr{J}_{\boldsymbol{v}_{CM1}} &= \begin{bmatrix} -p_{CM1_y} & 0 & 0 \\ p_{CM1_x} & 0 & 0 \\ 0 & 0 & 0 \end{bmatrix}, \\ \mathscr{J}_{\boldsymbol{v}_{CM2}} &= \begin{bmatrix} -p_{CM2_y} & p_{B_y} - p_{CM2_y} & 0 \\ p_{CM2_x} & p_{CM2_x} - p_{B_x} & 0 \\ 0 & 0 & 0 \end{bmatrix}, \\ \mathscr{J}_{\boldsymbol{v}_{CM3}} &= \begin{bmatrix} -p_{CM3_y} & p_{B_y} - p_{CM3_y} & p_{C_y} - p_{CM3_y} \\ p_{CM3_x} & p_{CM3_x} - p_{B_x} & p_{CM3_x} - p_{C_x} \\ 0 & 0 & 0 \end{bmatrix} \end{aligned} \tag{38}$$

Coordinates of points of interest in (38) can be obtained by direct kinematics. As regard the centers of mass, they are taken as shown in Fig. 4. In particular, CM_1 is placed at the connection between the boom and the first actuator; CM_2 is considered on the segment connecting C and M, at a distance $3a_4/5$ from C; for the bucket, it is assumed all the mass is concentrated in the teeth, at the point CM_3. One has:

$$\begin{aligned}
\boldsymbol{p}_B &= \begin{bmatrix} a_1 c_1 \\ a_1 s_1 \\ 0 \end{bmatrix}, \\
\boldsymbol{p}_{CM1} &= \begin{bmatrix} l_2 \cos(\theta_1 + \xi_1) \\ l_2 \cos(\theta_1 + \xi_1) \\ 0 \end{bmatrix}, \\
\boldsymbol{p}_{CM2} &= \begin{bmatrix} p_{Cx} - \frac{3}{5} a_4 \cos(\theta_1 + \theta_2 - \alpha_4) \\ p_{Cy} - \frac{3}{5} a_4 \sin(\theta_1 + \theta_2 - \alpha_4) \\ 0 \end{bmatrix}, \\
\boldsymbol{p}_{CM3} &= \begin{bmatrix} a_1 c_1 + a_2 c_{12} + a_3 c_{123} \\ a_1 s_1 + a_2 s_{12} + a_3 s_{123} \\ 0 \end{bmatrix}
\end{aligned} \tag{39}$$

As regard the angular velocity, it is clear that:

$$\boldsymbol{\omega}_1 = \dot{\theta}_1 \widehat{\boldsymbol{k}}, \boldsymbol{\omega}_2 = \left(\dot{\theta}_1 + \dot{\theta}_2\right) \widehat{\boldsymbol{k}}, \boldsymbol{\omega}_3 = \left(\dot{\theta}_1 + \dot{\theta}_2 + \dot{\theta}_3\right) \widehat{\boldsymbol{k}} \tag{40}$$

where $\widehat{\boldsymbol{k}}$ identifies the unit vector of axis x. Moreover, since $\boldsymbol{\omega}_i$ is aligned with $\widehat{\boldsymbol{k}}$, the triple product $\boldsymbol{\omega}_i^T \boldsymbol{I}_i \boldsymbol{\omega}_i$ reduces simply to $I_{i,z}$ times the square of the magnitude of the angular velocity.

3.3. Static force analysis

Manufacturers publish the maximum digging force of the excavator, measured or calculated according to the standards. In particular, ISO 6015 [30] provide procedures for measurement of the maximum tool force, depending on the actuated cylinder; for instance, the maximum bucket or arm forces are obtained by operating independently the related cylinders and by positioning the measuring device tangential to the arc described by the bucket lip. As the actual force at the teeth depends on the configuration of the excavator, a series of preliminary tests shall be conducted by varying the stroke of the cylinders in order to identify the optimum position corresponding to the maximum force. The mentioned approach has some limitations. In practice, finding the optimum position is a demanding operation, that can be prone to error and time-consuming. Moreover, actuating the arm or the bucket cylinder at time is not realistic in a worst-case scenario, where the operation may involve the use of all cylinders [31], causing reaction force on the bucket lip in any direction. Another possibility is to calculate bucket and arm forces with SAE formula [32]. However, it does not consider the weight of the components and still suffers from similar limitations mentioned for the ISO, as it considers only arm and bucket cylinders to be activated.

An analytic method for the estimation of the effective digging force is described in [33]. The method consists in modeling the excavator kinematic chain and calculating the digging force through static, considering the entire workspace and all the possible boundaries due to the stability of the excavator, as well as the working ranges of the driving mechanism. Starting from [33], in this section a simplified formulation which best fits the present case is described. The purpose is to give a handy tool for the estimation of the digging force that overcomes the limitations of the standards and that is more focused on the study of the interaction with buried

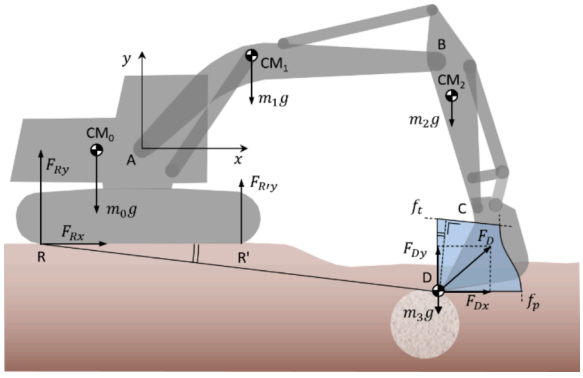

Fig. 7. Excavator equilibrium analysis during digging operation.

pipes.

External interference incidents caused by excavators happen when drivers operate near gas pipelines that are not exposed. Let $\boldsymbol{F}_D = \left[F_{Dx} F_{Dy} 0\right]^T$ denote the resistive force, i.e. the force exerted by the tube to the bucket lip. With a similar meaning, the digging force has the same magnitude of the resistive force and opposite direction. By considering pipes that range from 400 mm to 1200 mm diameter [34], it is legit to assume the contact on the top half of the tube, i.e. $F_{Dy} > 0$. In addition, the following hypothesis are made for the model of contact force: towards one-self operation (that translates into $F_{Dx} > 0$), digging from the track plane down, non-deformable soil and absence of slippage. Concerning assumptions on soil condition and interaction, it must be noticed that they are in line with a conservative approach. For instance, the maximum digging force in the case of a soft soil can be less than or equal to that calculated with non-deformable ground; similarly, the presence of slip would reduce the reaction force with the ground and result in a lower excavation force.

The external forces acting on the excavator are reported with solid lines in Fig. 7. Concerning the limit conditions, $\boldsymbol{F}_D$ is bounded by functions f_t and f_p, that represent the tipping limit and the hydraulic circuit limit, respectively. The tipping limit corresponds to the rotation of the excavator about R, which means that the reaction at the front is $F_{R'y} = 0$; in this case, for a given digging position, the $\boldsymbol{F}_D$ component in the direction perpendicular to the segment $\overline{RD}$ is denoted as F_t and is constant, i.e. the tipping limit function f_t is a straight line. On the other hand, determining the curve f_p is not straightforward. This can be done with the following numerical scheme, by checking the pressure of the cylinders until it exceeds the rated maximum value.

For each digging pose defined by $\boldsymbol{p}_D$ and ϕ, the configuration of the excavator is obtained through inverse kinematics. Thus, given F_{Dx} and F_{Dy}, the static equilibrium of the excavator can be solved to find the internal loads across the structure. In the free-body diagrams in Fig. 8, external and internal loads are drawn. The subscript of each loads indicates the relative joint and the direction. For instance, F_{Ax} and F_{Ay} are the x axis and the y axis components, respectively, of the force $\boldsymbol{F}_A$ acting on the joint A.

The problem in Fig. 8 consists of 29 unknowns. The same number of equations can be written considering the equilibrium of each body. The solution to the problem is reported in Appendix A. Such a solution is obtained for a given pose and a given resistive force. The maximum resistive force is computed by cycling for $\boldsymbol{p}_D$ and ϕ on all the possible configurations, as well as by spanning F_{Dx} and F_{Dy} within the limit conditions. The possible configurations $\boldsymbol{p}_D$ and ϕ are the ones that admit a solution to the inverse kinematic problem and that correspond to a stroke of the actuators within the range given by manufacturers. The tipping limit condition can be calculated as in Appendix A. The limit of the hydraulic circuit can be identified solving for the static equilibrium, considering the force exerted by the actuators and the radius of the cylinders, denoted as r_1, r_2 and r_3, to find the corresponding operating pressures p_1, p_2 and p_3. The radius of the cylinders and the maximum pressures are given by datasheet. In Table 1 the pseudocode for computation of the digging force is shown.

3.4. Example of maximum static force and kinetic energy calculation

In this section, the analysis of the digging force of a medium size excavator modelled with specifications taken from [35] is proposed to show how the code in Table 1 can be used to compute the maximum digging force and to find the conditions that limit the digging force for each configuration.

The analysis of the digging force of the excavator in the plane identified by the xy axis with origin in A is reported in Fig. 9, where the color bar indicates the digging force in kN. As the digging force depends on the angle between the bucket and the horizontal direction, too, this diagram is obtained considering the greatest force over the possible ϕ, given a digging position. In particular, the possible ϕ are the ones that admit a solution for the inverse kinematics, in the range defined by $\phi_{min} = \pi + \gamma$ (bottom of the bucket aligned with the horizontal direction) and $\phi_{max} = 2\pi$ (front of the bucket aligned with the horizontal direction). As can be seen, digging

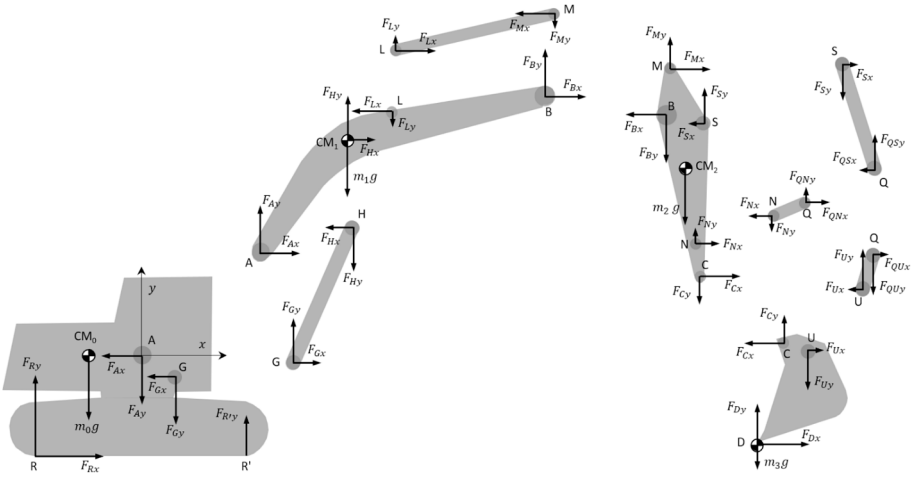

Fig. 8. Static equilibrium of the excavator.

Table 1
Pseudocode for digging force computing.

From datasheet: $p_{Dx,min}$, $p_{Dx,max}$, $p_{Dy,min}$, $p_{Dy,max}$, ϕ_{min}, ϕ_{max}
$l_{GH,min}$, $l_{GH,max}$, $l_{LM,min}$, $l_{LM,max}$, $l_{SQ,min}$, $l_{SQ,max}$
$p_{1,max}$, $p_{2,max}$, $p_{3,max}$, r_1, r_2, r_3,
Choose: Δp_{Dx}, Δp_{Dy}, $\Delta\phi$, ΔF_{Dx}, ΔF_{Dy}
for $p_{Dy} = p_{Dy,min}$ to $p_{Dy} = p_{Dy,max}$ with increment Δp_{Dy}
  for $p_{Dx} = p_{Dx,min}$ to $p_{Dx} = p_{Dx,max}$ with increment Δp_{Dx}
    for $\phi = \phi_{min}$ to $\phi = \phi_{max}$ with increment $\Delta\phi$
      Inverse kinematics $\rightarrow \boldsymbol{q}$
      Direct kinematics $\rightarrow l_{GH}$, l_{LM}, l_{SQ}
      if $l_{GH,min} \le l_{GH} \le l_{GH,max}$ and $l_{LM,min} \le l_{LM} \le l_{LM,max}$ and $l_{SQ,min} \le l_{SQ} \le l_{SQ,max}$
        for $F_{Dy} = 0$ to $F_{Dy} = F_t$ with increment ΔF_{Dy}
          while $p_1 \le p_{1,max}$ and $p_2 \le p_{2,max}$ and $p_3 \le p_{3,max}$ and $F_{R'y} \ge 0$
          $F_{Dx} = F_{Dx} + \Delta F_{Dx}$
          $\boldsymbol{x} = \boldsymbol{A}^{-1}\boldsymbol{b} \rightarrow \boldsymbol{F}_G, \boldsymbol{F}_L, \boldsymbol{F}_S, \boldsymbol{F}_R$
          $p_1 = \|\boldsymbol{F}_G\|/(\pi r_1^2)$, $p_2 = \|\boldsymbol{F}_L\|/(\pi r_2^2)$, $p_3 = \|\boldsymbol{F}_S\|/(\pi r_3^2)$
          $\boldsymbol{F}_D = [F_{Dx} F_{Dy} 0]^T$
          end
        end
      end
    end
  end
end

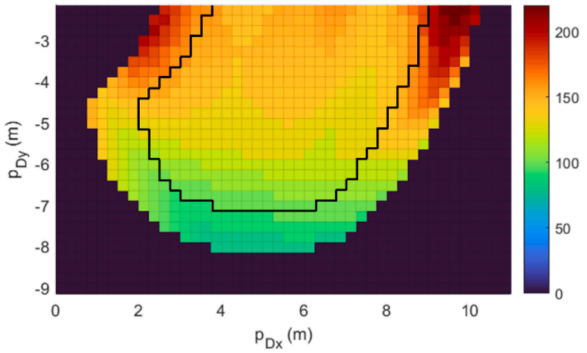

Fig. 9. Analysis of the digging force of the medium size excavator in the x-y plane.

forces are greater at the boundaries of the workspace in the proximity of $p_{Dy} = 0$. The configuration corresponding to the maximum digging force is $p_{Dx} = 9.5\text{m}, p_{Dy} = 0, \phi = 2\pi$. In general, safe procedures consider operating in the middle of the workspace to improve machine stability. For instance, the maximum digging forces calculated according to the standards is related to configurations that are

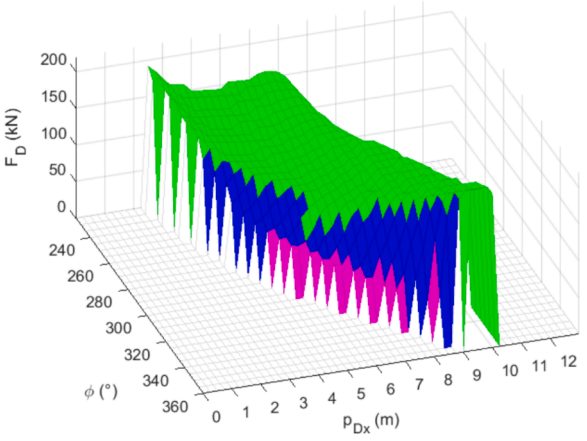

Fig. 10. Analysis of the digging force at $p_{Dy} = -d$.

far from the workspace boundaries. For this, in the results section, the analysis of the maximum force will distinguish two cases: the possible range and the operative range. The operative range is obtained by reducing the possible range. As in the literature there is no evidence of how much the operative range differ from the possible range, in this work a reduction of 30 % has been chosen. Results will show that this gives an operative range where digging forces are similar to rated forces given by manufacturers. For instance, the contour of the operative range is indicated in Fig. 9 with an offset line with respect to the possible range boundaries. The distinction of the two ranges will be used in the result section to indicate preventive actions that can be taken in order to mitigate the risk of failure.

Fig. 10 shows the digging force for $p_{Dy} = 0$, for different values of p_{Dx} and ϕ. The different colors indicates which is the limit condition that bounds the greatest digging force for each configurations. The tipping limit is indicated with magenta, while colors red, green and blue indicates if the maximum pressure is achieved in the boom, arm or bucket cylinders, respectively. In the case, it can be observed that the greatest force for each configuration at $p_{Dy} = 0$ is not limited by the pressure of the boom cylinder, while the maximum force is obtained when the arm cylinder reaches the pressure limit.

The diagram of the admissible resistive forces in the configuration of maximum digging force is shown in Fig. 11. The maximum force is obtained for $F_{Dx} = 4.52$kN and $F_{Dx} = 220$kN and is limited by the pressure of the arm cylinder. However, as can be seen, for this configuration there are admissible pairs of F_{Dx} and F_{Dy} for which the resistive force is limited by the pressure of the boom cylinder.

Finally, in Fig. 12 shows the kinetic energy of the excavator in function of the digging position. Even in this case, the graph is obtained by considering at each point the greatest value of the kinetic energy over the possible ϕ. It can be noticed that the kinetic energy increases at the farthest boundary of the workspace, for deeper digging positions. Similarly to the static force analysis, the distinction between possible range and operative range will be used in the results section for the study of the maximum kinetic energy.

4. Pipe damage model

The relationship between denting force and denting diplacement was taken from the model proposed by Gresnigt et al. [10,11]. This is an analytical/heuristic two-dimensional model, in which the total response is assumed to consist of three parts (elastic, plastic and membrane). It has the advantage of providing a simple analytic formulation within an accurate modeling of the phenomena, thus avoiding FE computation, in the presence of internal pressure, whose effects were obtained by virtual work principle; the three-dimensional effects are taken in account through appropriate correcting parameters. In the following the adopted formulas and a brief description are presented for the three parts, focusing on the relation between denting force F and denting displacement δ.

1) Elastic solution: the denting force follows the relation:

$$F = F_e = \frac{EI}{0.149R^3\sqrt{\alpha_{rr}}}B_e\delta \tag{41}$$

where EI is the ring bending stiffness of the pipe wall per unit length, R the pipe radius, $B_e = 1.33R\sqrt{(R/t)} + b$ the "equivalent pipe length", b is the width of the tooth, t the pipe thickness, α_{rr} is the pressure factor calculated as:

$$\alpha_{rr} = \frac{p_{cr}}{p_{cr} + p} \tag{42}$$

Where p is the actual internal pressure (positive when internal), $p_{cr} = 3EI/R^3$ is the critical buckling external pressure of a uniformly pressurized ring, so that $\alpha_{rr} = 1$ when no internal pressure is present. F is linear with δ.

2) Plastic solution: the model developed by Gresnigt et al. is based on an equally spaced four hinge plastic mechanism under plane-strain conditions. From this, the limit plastic load for the elastic behavior is calculated as:

$$F = F_p + F_{pi} \tag{43}$$

where F_p and F_{pi} are the plastic ring mechanism force, independent of δ and the internal pressure effect, linear with δ, defined as follows:

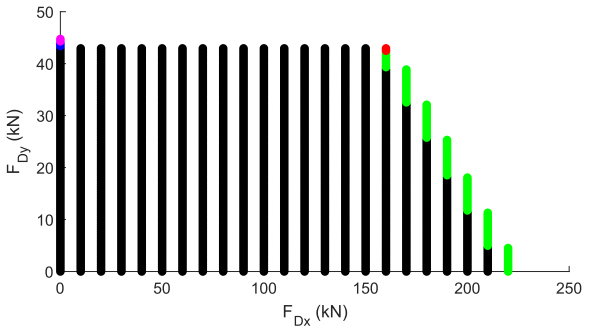

Fig. 11. Diagram of the allowable resistive forces at the configuration of the maximum digging force for the excavator pc240.

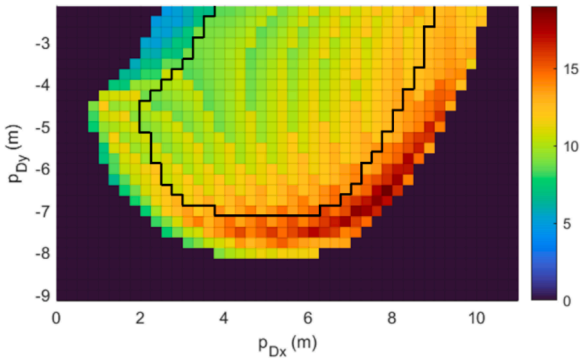

Fig. 12. Analisys of the kinetic energy of the pc240 excavator in the x-y plane.

$$F_p = 1.15\frac{\sigma_0 t^2}{R}\left[1 - 0.75\left(\frac{\sigma_r}{\sigma_0}\right)^2\right]B_p S_B \tag{44}$$

$$F_{pi} = 2pB_{pi}\delta \tag{45}$$

where σ_0 is the yield stress, $\sigma_r = pR/t$ the hoop stress due to internal pressure, $B_p = 0.80R\sqrt{R/t} + b$, and $S_B = R/(R - 0.35b)$ for $b \leq 2R$ that accounts for local effects due to the orientation of the wedge, and is equal to 1 when a longitudinally oriented wedge is applied; $B_{pi} = 0.4\alpha_{rr}R\sqrt{R/t} + b$. In absence of internal pressure,the displacement increase occurs without change in the applied load; the internal pressure causes the denting force increase to linearly increase the dent depth.

3) Membrane solution: the membrane effect follows the plastic deformation and are due to the stretching of the pipe meridians which resist the denting force. The upper limit of the plastic phase occurs when the applied load equals to

$$F = F_m + F_{pi} \tag{46}$$

where F_m is the required lateral force for membrane deformation, and is equal to

$$F_m = \frac{0.2\sigma_0 Rt\sqrt{\frac{R}{t}}\delta}{\sqrt{\delta^2 + \frac{R^3}{64t}}}S_B \tag{47}$$

The relation between F and δ is nonlinear in the membrane phase.

The effect of the internal pressure is shown in Fig. 13. The curves are obtained for a DN600 pipe for gas transmission, made of L415 steel, with $t = 11$mm, and considering a tooth width $b = 40$mm. The increase of pressure implies an increase of both the denting force

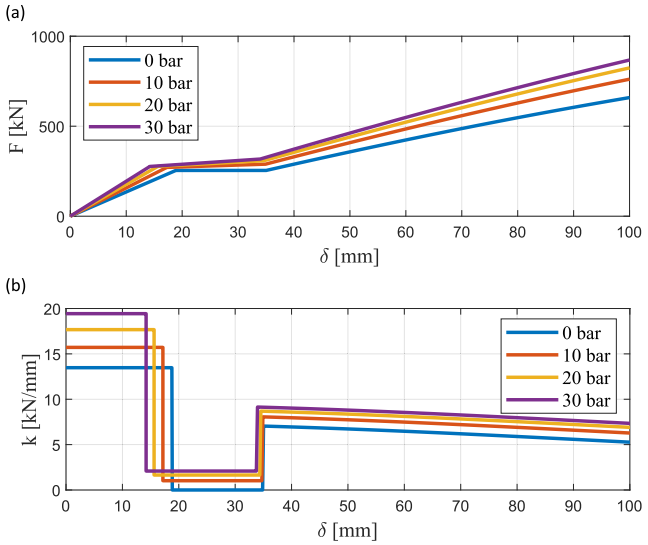

Fig. 13. Comparison for different pressure level: a) denting force versus dent depth; b) equivalent stiffness of the dented tube versus dent depth.

required for the same denting displacement, and an increase of the equivalent stiffness of the dented tube calculated as:

$$k_{eq} = \frac{\Delta F}{\Delta \delta} \tag{48}$$

This trend is in line with the outcomes of [10]. In fact, an increase of pressure cause a decreasing of α_{rr}, which results in a greater F_e for a given δ from (41), thus in a greater stiffness. It can also be recognized the three-stage behaviour of the model and the effect on the denting force of the pressure during the plastic stage, for which the slope of the linear relation increases with the pressure because of the additional term F_{pi} in (43).

The curves described by equations (41)–(48) were compared to experimental tests and showed agreement between the data and the analytic model, as reported in [10,11].

5. Excavator and pipe model coupling

In this section the simplified dynamic model of the coupled behavior between excavator and the pipe during denting is presented. For sake of simplicity it is assumed that during denting the boom rotates about the first hinge under the action of the first actuator, such as it happens during large displacement operations. In Fig. 14 the free-body representation of the excavator and pipe system during a denting event is depicted: θ_1 is the rotation angle of the boom around the first hinge, assumed as a reference point, l is the horizontal distance between the hinge and the contact point where the denting takes place, k the overall stiffness of the system, δ the dent depth, F the static force at the excavator tooth in the chosen configuration. The kinetic energy theorem can be written taking in account of the excavator force, the stiffness and the damping effects:

$$\frac{dK}{dt} = \frac{d(I\omega_1)}{dt} = Fl - k(\delta)\delta l - \beta\dot{\delta} l \tag{49}$$

where $\omega_1 = \dot{\theta}_1$, I is the total inertial moment of the boom around the hinge, calculated with the Huygens-Steiner theorem

$$I = \sum_{i=1}^{n} \left(I_i + m_i d_i^2\right) \tag{50}$$

and I_i is the center of mass inertia moment of the i-th arm, m_i its mass and d_i the distance of the i-th center of mass from the hinge, n the number of arms of the boom. The (49) can then be rewritten in the following form:

$$I\ddot{\theta} = Fl - k(\delta)\delta l - \beta\dot{\delta} l \tag{51}$$

The system stiffness k is calculated considering the pipe and the boom stiffness as in series, so

$$\frac{1}{k} = \frac{1}{k_{eq}} + \frac{1}{k_{ex}} \tag{52}$$

where k_{eq} is calculated through (48), and the excavator boom stiffness k_{ex} is calculated by the empirical relation

$$k_{ex} = C \bullet m_{ex} \tag{53}$$

where m_{ex} is the total excavator mass in kilograms, and $C(N/m/kg)$ is a correlation factor determined experimentally and here set at

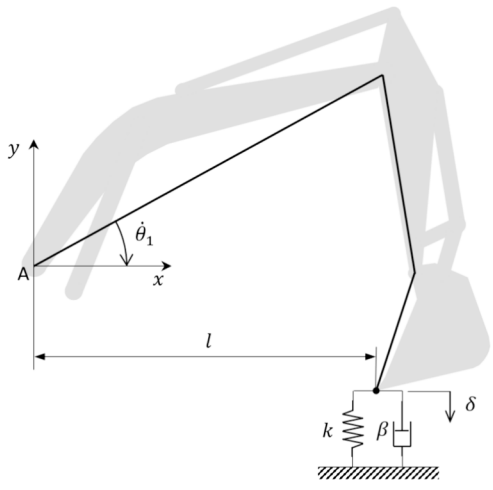

Fig. 14. Simplified free-body scheme of the excavator beam (in blue) during a denting event.

$C = 279\left(\frac{N}{m \bullet kg}\right)$.

The damping factor β can be chosen in order to make the system critically damped:

$$\beta = 2\sqrt{\frac{Ik}{l^2}} \tag{54}$$

As for the static force calculation, it is pointed that equation (51) consider a non-deformable soil and is part of the conservative approach of this study. In fact, a soft soil would intervene as a stiffness and damping in series with the ones of pipe and excavator, resulting in a greater dissipation of kinetic energy, and therefore less denting.

The system described by (51) is then integrated in a simulating environment (Matlab/Simulink) to evaluate the final value of δ after an excavator impact. The simplified impact model require as initial condition for integration the angular velocity of the boom. This is computed introducing the equivalent angular velocity, which is defined considering the maximum kinetic energy:

$$\dot{\theta}_{1,eq} = \sqrt{2 \bullet \frac{E_{k,max}}{I}} \tag{55}$$

The introduction of the equivalent angular velocity permits to use the simplified model of contact, but incorporating the effect of motion of the three actuators. This is a worse scenario, as $\dot{\theta}_{1,eq} > \dot{\theta}_{1,max}$, where $\dot{\theta}_{1,max}$ is the maximum angular velocity of the boom that can be reached by datasheet, and that depends on the boom cylinder size and on the hydraulic oil flow rate.

6. Results and discussion

The aforementioned methods is applied to excavator models from various manufacturer, including Caterpillar, Kobelco, Volvo and Hyundai. Table 2 shows their main features related to the size, the hydraulic circuit and the ISO digging forces according to manufacturer catalogue. Other kinematic and inertial properties for modelling have been taken from related datasheets. Excavators are identified with an ID, with the letter referring to the their size. For instance, according to [36], excavators can be classified into 3 groups by their weight: small (S) $<$ 15 ton, medium (M) up to 40 ton, and large (L) $>$ 40 ton.

In Fig. 15a the maximum static force of excavator of various size is shown. Computed forces distinguished between the possible range and the operative range. As the possible range includes regions close to the workspace boundary, forces are greater than the ones calculated with the operative range. Results obtained by simulation are compared with the rated ISO maximum force by datasheet, when available. Forces measured according to ISO standards consider excavator in an operative configuration, in fact they are closer to the one calculated by simulation within the operative range. In the same graph, also the relationship between excavator mass and the maximum digging force by Lu et al. is shown [36]. The curve by Lu et al. is based on regression analysis of 321 types of excavators from 20 manufacturers. Overall, the maximum forces related to the operative range match the rated force and the relationship by Lu et al. On the other hand, force analysis within the possible range over-estimates the maximum force.

Fig. 15b shows results in terms of maximum kinetic energy. In this case, the trend is not well defined. In fact, the difference of mass for different size excavator is mostly due to the main body, rather than to the arm. Moreover, kinetic energy is also related to rotational velocity of the arm bodies, that is a function of the rod velocity at a given configuration. Thus, results are affected by more variables.

Maximum static force and kinetic energy are coupled with the pipe model to study the denting displacement δ that an excavator can cause. In particular, the results are provided by means of dent charts, i.e. graphs in which the ordinate contains the denting displacement and the abscissa a parameter of interest, such as the size of the excavator expressed in mass, or the size of the pipe represented by its diameter.

For example, Fig. 16 shows the maximum denting displacement for a DN600 pipe for gas transmission, made of L415 steel, with t = 11 mm. The internal pressure is supposed to be null in order to consider the worst case scenario. In the same graph, the plastic limit δ_p of the pipe, i.e. the denting displacement for which one have the transition to plastic region according to Gresnigt et al., is reported with a dashed line. For instance, above the value δ_p, the deformation is permanent and therefore damage occurs in the form of dent. Excavator models whose maximum denting displacement is less than the plastic limit can be safely used for digging, i.e. S1, S2, M2, M4.

Table 2
Excavator models, listed in ascending order of the total mass.

ID	Mass [kg]	Max hydraulic pressure [Mpa]	Max total hydraulic flow [L/min]	Cylinder bore (boom, arm, bucket) [mm]	Max ISO digging force [kN]
S1	13 400	28.5	240	105, 115, 95	N/A
S2	14 970	32.4	248	105, 120, 100	96.6
M1	20 080	35	440	120, 140, 125	152
M2	20 250	35	370	120, 130, 110	N/A
M3	24 050	31.4	460	135, 140, 130	173
M4	24 600	37	475	130, 140, 130	175
M5	33 000	30	546	145, 165, 145	N/A
L1	44 800	31.4	740	170, 190, 160	292
L2	47 000	35	734	160, 190, 160	268

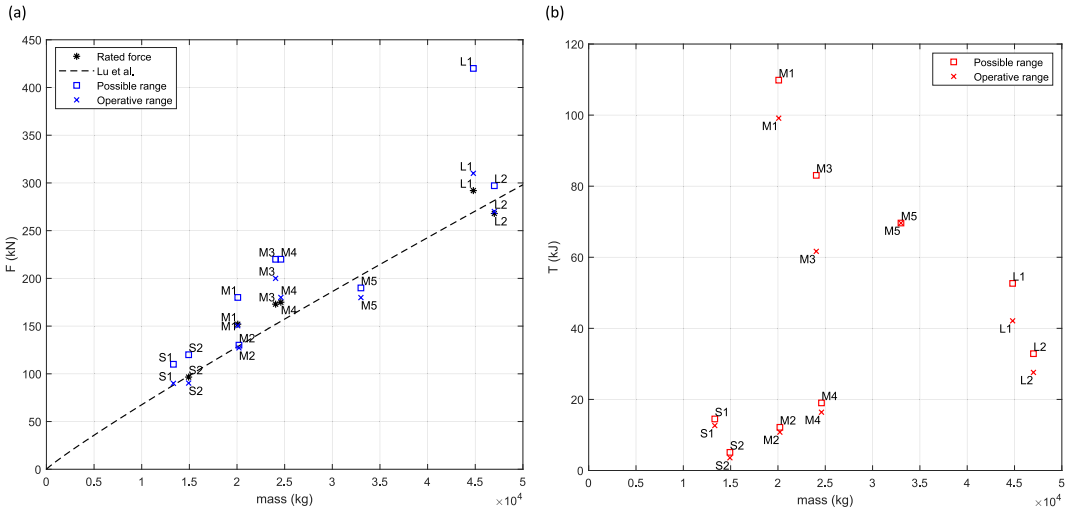

Fig. 15. Analysis for excavators of various size and manufacturers: (a) maximum static force; (b) maximum kinetic energy.

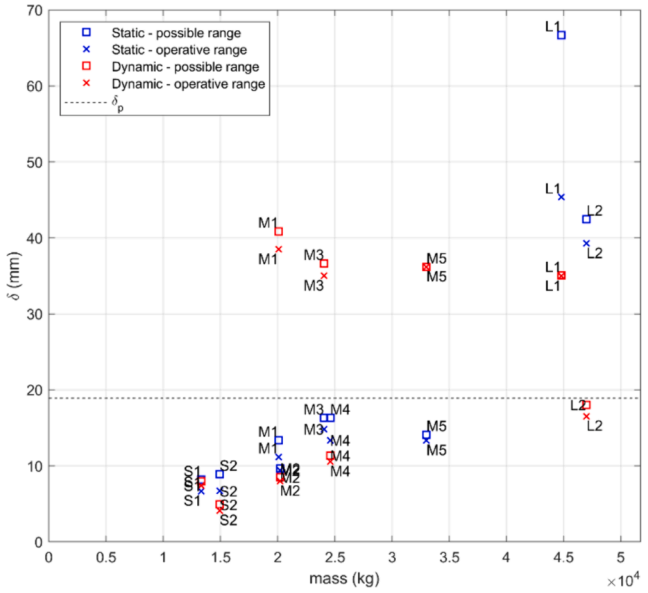

Fig. 16. Excavator mass versus maximum denting displacement for a DN600-L415 steel pipe with null internal pressure.

Fig. 17 show the effect of pipe features on maximum denting displacement for one representative excavator of each category size. Data are obtained considering DN450 to DN750 non-pressurized pipes used for gas transmission, characterized by L415 steel and t = 11. This graphs can provide an aid to assign to an excavator a set of pipes on which it can operate without producing a plastic deformation. In this case, the S2 excavator can safely operate with each pipe. Concerning the M3 excavator, it can potentially damage all pipes. However, for DN≥600, it can be noticed that a dent is related to the possible range. In order to make M3 suitable for DN≥600, the preventive action could be to limit the actuator stroke at a control level, so to make possible to work only in the operative range.

The same approach can be used for L2 excavator. Notice that for large excavators dynamic impact cause less damage than a static contact. This happens because the larger the size, the greater the maximum static force; however, this is not true for the kinetic energy.

7. Conclusions

A novel method for the selection of the excavator to employ for a safe operation in the proximity of gas pipe lines has been proposed. The method is based on coupling excavator and pipe models to quantify the damage produced by the excavator on the pipe in case of accidental contact.

From a practical point of view, what was desired was a tool to increase the safety of operators during the excavation phase and to

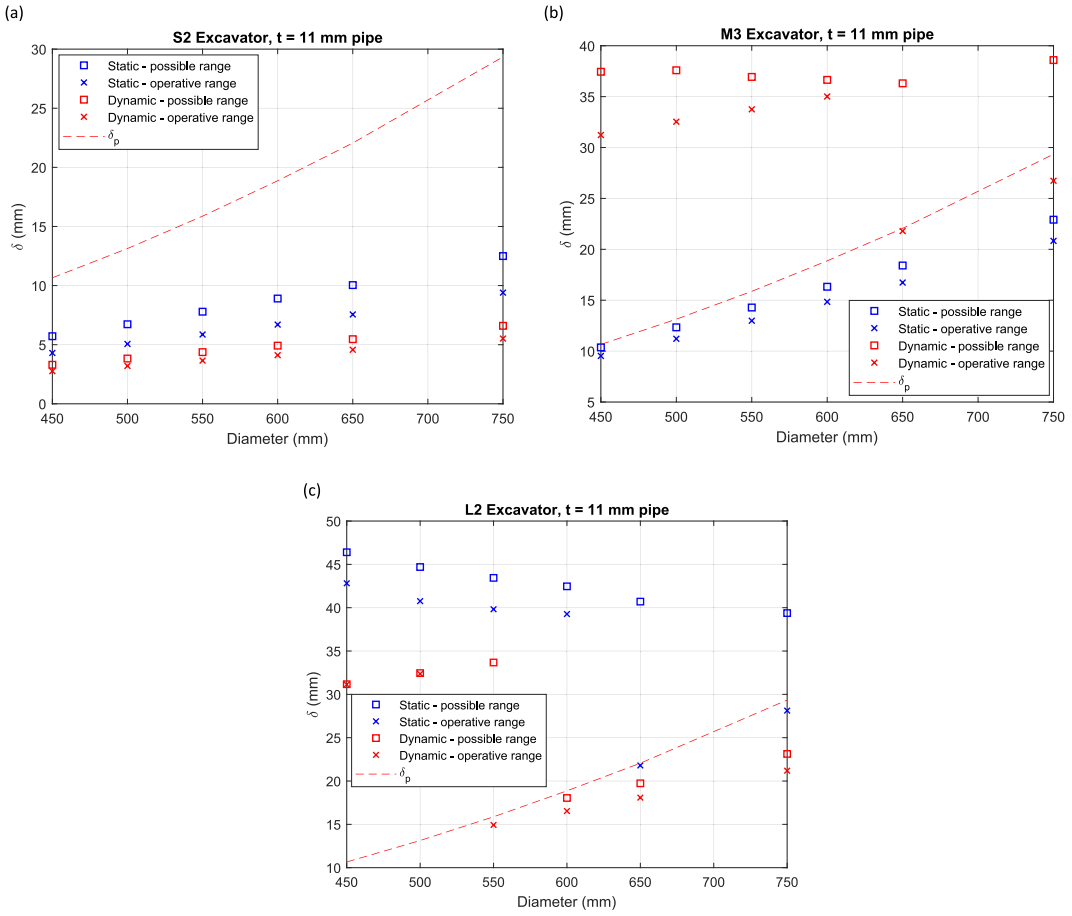

Fig. 17. Maximum denting displacement of excavators on L415 steel pipe of different sizes: (a) S2 excavator: (b) M3 excavator; (c) L2 excavator.

preserve the integrity of the network. From the history of accidents involving gas pipes, it has in fact emerged that one of the major causes of pipe damage is impact with excavators, despite numerous precautions. For this reason, during the initial phase of setting up the method, an attempt was made not to neglect anything, even the least probable scenarios. For example, both static and dynamic contacts were considered, as they reflect two operational scenarios in which bucket-pipe contact can occur, namely during excavation, where there are low velocities, or during the handling of machinery near the excavation point, where the dynamic effect may not be negligible. Following this logic, the models that make up the method are set up so that the worst case can be identified, i.e. so that the maximum forces of all those possible at the moment of impact can be calculated.

The excavator model allows to calculate the maximum force at the bucket tooth, in the case of static and dynamic contact. The maximum static digging force is computed by taking into account actuator ranges in terms of length and pressure, as well as tipping condition. The dynamic contact considers the maximum kinetic energy, that is computed starting from maximum actuator velocities and inertial properties of the moving bodies. As the static force and the kinetic energy depend on the configuration, the method relies on a practical numerical scheme to find maximum values within the excavator workspace. The numerical scheme have been implemented in Matlab by considering various excavator types. The analysis has shown that computed maximum digging forces within the operative range of excavators match rated forces by manufacturer datasheets. Furthermore, having considered different excavator sizes between 13 and 47 tonnes, it was possible to identify the trend of maximum static force as a function of machine size, which in fact mirrors that of Lu et. Al [36].

The pipe model give denting response of pressurized and non-pressurized tubes subjected to excavation loads, and is based on equations by Gresnigt et al., that consist in a three-stage behaviour that is in agreement with experimental data. The advantage of the Gresnigt equations is that, in addition to geometrical characteristics, it can take into account boundary conditions such as internal pressure, impact direction or tooth width.

Excavator and pipe are coupled by solving for damped contact equations, that consider also pipe and excavator stiffnesses. A contact model is introduced, that consider the boom rotating with an equivalent angular velocity, computed by the maximum kinetic energy of the excavator.

Simulation results have shown that dent can be related to static or dynamic contacts, depending on the excavator. Using a common DN600 pipe as a practical example, the results show that of the excavators considered, small excavators do not damage the pipe,

medium excavators damage the pipe after a dynamic impact, while for large excavators the static force is more critical. This result is further highlighted by the subsequent analysis of deformation as the pipe diameter varies, carried out on three representative excavators.

The results were not limited to distinguishing between static and dynamic contact. In fact, it was found that by carrying out an analysis based on the entire workspace of the excavator, i.e. the possible range, from the base of the track downwards, it was easier to find configurations in which the force or kinetic energy was such that the pipe was plastically deformed. However, since these configurations are often at the boundary of the workspace, it was decided to also study the operative range, i.e. to concentrate the analysis on the configurations normally used during excavation, which can usually be traced back to the central zone of the workspace. In the operative range, forces are lower so it is more difficult to damage the pipe. This last result led to the idea of a preventing action for mitigating the risk of failure, based on the possibility to limit the excavator to the operative range with the control system.

The proposed method is theoretical and stands on equations that are in line with experimental data (excavator and pipe models) and other that have not yet been validated (contact model), but the first results seem to be coherent with the in-field experience and approaches of the TSOs.. Based on the results of the work presented, the intention is to obtain confirmation from the field to provide those planning excavations with a more reliable tool to ensure the safety of the operators. As of 2024, Snam has started work on the replacement of several gas transmission pipelines. The idea is to take advantage of the replacement work to have a large number of old pipes on which to carry out tests, thus reducing the cost of an experimental campaign that requires a large-scale assessment. Work is currently underway to define the experimental campaign and to fine-tune the instrumentation for data collection, which will involve not only several pipes with different diameter and thickness, but also several excavators. The experiments will involve the Politecnico di Torino and Snam and will start in the second half of 2024.

CRediT authorship contribution statement

Matteo Melchiorre: Writing – review & editing, Writing – original draft, Visualization, Validation, Software, Methodology, Investigation, Formal analysis, Data curation, Conceptualization. **Luca Bacchi:** Writing – review & editing, Writing – original draft, Validation, Supervision, Project administration, Methodology, Funding acquisition, Formal analysis, Data curation, Conceptualization. **Pierpaolo Palmieri:** Validation, Software, Methodology, Investigation, Formal analysis. **Andrea Ruggeri:** Writing – original draft, Validation, Software, Methodology, Investigation, Formal analysis, Data curation. **Laura Salamina:** Validation, Software, Methodology, Investigation, Formal analysis. **Stefano Mauro:** Writing – review & editing, Validation, Supervision, Resources, Project administration, Methodology, Funding acquisition, Formal analysis, Conceptualization.

Declaration of competing interest

The authors declare the following financial interests/personal relationships which may be considered as potential competing interests: Matteo Melchiorre, Pierpaolo Palmieri, Andrea Ruggeri, Laura Salamina, Stefano Mauro reports financial support and writing assistance were provided by Snam SPA. If there are other authors, they declare that they have no known competing financial interests or personal relationships that could have appeared to influence the work reported in this paper.

Data availability

The authors do not have permission to share data.

Acknowledgements

The work was financially supported by Snam SPA.

Appendix A. Static equilibrium of the excavator

From Figure 9, the following equations can be written for the equilibrium of the excavator:

Base

$$\begin{aligned} &\rightarrow \quad -F_{Ax} - F_{Gx} + F_{Rx} = 0 \\ &\uparrow \quad -F_{Ay} - F_{Gy} + F_{Ry} - F_{R`y} - m_0 g = 0 \\ &\circlearrowleft A \; -F_{Gx} l_{AGy} - F_{Gy} l_{AGx} + F_{Rx} l_{ARy} - F_{Ry} l_{ARx} + F_{R`y} l_{AR`x} + m_0 g l_{ACM_0 x} = 0 \end{aligned} \tag{56}$$

Boom

$$\begin{aligned} &\rightarrow \quad F_{Ax} + F_{Bx} + F_{Hx} - F_{Lx} = 0 \\ &\uparrow \quad F_{Ay} + F_{By} + F_{Hy} - F_{Ly} - m_1 g = 0 \\ &\circlearrowleft A \; -F_{Bx} l_{ABy} + F_{By} l_{ABx} - F_{Hx} l_{AHy} + F_{Hy} l_{AHx} + F_{Lx} l_{ALy} + F_{Ly} l_{ALx} - m_1 g l_{ACM_1 x} = 0 \end{aligned} \tag{57}$$

Arm

$$\begin{aligned} &\rightarrow \quad -F_{Bx} + F_{Cx} + F_{Mx} + F_{Nx} - F_{Sx} = 0 \\ &\uparrow \quad -F_{By} - F_{Cy} + F_{My} + F_{Ny} + F_{Sy} - m_2 g = 0 \\ &\circlearrowleft B \; F_{Cx} l_{BCy} - F_{Cy} l_{BCx} - F_{Mx} l_{BMy} + F_{My} l_{BMx} + F_{Nx} l_{BNy} + F_{Ny} l_{BNx} - F_{Sx} l_{BSy} + F_{Sy} l_{BSx} - m_2 g l_{BCM_2 x} = 0 \end{aligned} \tag{58}$$

Bucket

$$\begin{aligned} &\rightarrow \quad -F_{Cx} + F_{Dx} + F_{Ux} = 0 \\ &\uparrow \quad F_{Cy} + F_{Dy} - F_{Uy} - m_3 g = 0 \\ &\circlearrowleft C \; F_{Dx} l_{CDy} - F_{Dy} l_{CDx} + F_{Ux} l_{CUy} - F_{Uy} l_{CUx} + m_3 g l_{CCM_2 x} = 0 \end{aligned} \tag{59}$$

Actuator 1

$$\begin{aligned} &\rightarrow \quad F_{Gx} - F_{Hx} = 0 \\ &\uparrow \quad F_{Gy} - F_{Hy} = 0 \\ &\circlearrowleft G \; F_{Hx} l_{GHy} - F_{Hy} l_{GHy} = 0 \end{aligned} \tag{60}$$

Actuator 2

$$\begin{aligned} &\rightarrow \quad F_{Lx} - F_{Mx} = 0 \\ &\uparrow \quad F_{Ly} - F_{My} = 0 \\ &\circlearrowleft L \; F_{Mx} l_{LMy} - F_{My} l_{LMx} = 0 \end{aligned} \tag{61}$$

Actuator 3

$$\begin{aligned} &\rightarrow \quad F_{Sx} + F_{QSx} = 0 \\ &\uparrow \quad F_{Sy} - F_{QSy} = 0 \\ &\circlearrowleft Q \; - F_{Sx} l_{QSy} + F_{Sy} l_{QSx} = 0 \end{aligned} \tag{62}$$

Body NQ

$$\begin{aligned} &\rightarrow \quad -F_{Nx} + F_{QNx} = 0 \\ &\uparrow \quad -F_{Ny} + F_{QNy} = 0 \\ &\circlearrowleft N \; - F_{QNx} l_{NQy} + F_{QNy} l_{NQx} = 0 \end{aligned} \tag{63}$$

Body QU

$$\begin{aligned} &\rightarrow \quad -F_{Ux} + F_{QUx} = 0 \\ &\uparrow \quad F_{Uy} - F_{QUy} = 0 \\ &\circlearrowleft U \; - F_{QUx} l_{UQy} - F_{QUy} l_{UQx} = 0 \end{aligned} \tag{64}$$

Node Q

$$\begin{aligned} &\rightarrow \quad -F_{QNx} + F_{QSx} - F_{QUx} = 0 \\ &\uparrow \quad -F_{QNy} - F_{QSy} + F_{QUy} = 0 \end{aligned} \tag{65}$$

The lengths can be calculated as:

$$\begin{aligned} l_{AGx} &= -l_{AG}\cos(\varepsilon_1) \\ l_{AGy} &= l_{AG}\sin(\varepsilon_1) \end{aligned} \tag{66}$$

$$\begin{aligned} l_{ARx} &= l_{AR'x} = l_{RR'x}/2 \\ l_{ARy} &= d \end{aligned} \tag{67}$$

$$l_{ACM_0 x} = l_{RR'x}/4 \tag{68}$$

$$\begin{aligned} l_{ABx} &= a_1\cos(\theta_1) \\ l_{ABy} &= a_1\sin(\theta_1) \end{aligned} \tag{69}$$

$$\begin{aligned} l_{AHx} &= -l_{AH}\cos(\varepsilon_1 + \beta_1) \\ l_{AHy} &= -l_{AH}\sin(\varepsilon_1 + \beta_1) \end{aligned} \tag{70}$$

$$l_{ALx} = l_{AL}\cos\left[\theta_1 + \cos^{-1}\left(\frac{a_1^2 + l_{AL}^2 - l_{BL}^2}{2a_1 l_{AL}}\right)\right]$$
$$l_{ALy} = l_{AL}\sin\left[\theta_1 + \cos^{-1}\left(\frac{a_1^2 + l_{AL}^2 - l_{BL}^2}{2a_1 l_{AL}}\right)\right] \quad (71)$$

$$l_{ACM_1x} = l_{AH}\cos(\theta_1 + \xi_1) \quad (72)$$

$$l_{BCx} = p_{Cx} - p_{Bx}$$
$$l_{BCy} = p_{By} - p_{Cy} \quad (73)$$

$$l_{BMx} = l_{BM}\cos(\theta_1 + \xi_2)$$
$$l_{BMy} = l_{BM}\sin(\theta_1 + \xi_2) \quad (74)$$

$$l_{BNx} = l_{BMx} - l_{CN}\cos(\theta_1 + \theta_2 + \nu_4 + \beta_4 + \varepsilon_4 + \mu_4)$$
$$l_{BNy} = l_{BMy} + l_{CN}\sin(\theta_1 + \theta_2 + \nu_4 + \beta_4 + \varepsilon_4 + \mu_4) \quad (75)$$

$$l_{BSx} = l_{BNx} - l_{NS}\cos(\theta_1 + \theta_2 + \beta_3 + \beta_4 + \nu_4 + \varepsilon_4 - \rho_4)$$
$$l_{BSy} = l_{BNy} + l_{NS}\sin(\theta_1 + \theta_2 + \beta_3 + \beta_4 + \nu_4 + \varepsilon_4 - \rho_4) \quad (76)$$

$$l_{BCM_2x} = p_{CM2x} - p_{Bx} \quad (77)$$

$$l_{CDx} = p_{Cx} - p_{Dx}$$
$$l_{CDy} = p_{Cy} - p_{Dy} \quad (78)$$

$$l_{CUx} = -l_{CU}\cos(\theta_1 + \theta_2 + \beta_4 + \nu_4)$$
$$l_{CUy} = l_{CU}\sin(\theta_1 + \theta_2 + \beta_4 + \nu_4) \quad (79)$$

$$l_{CCM_2x} = l_{CDx} \quad (80)$$

$$l_{GHx} = -l_{GH}\cos(\alpha_1 + \beta_1 + \varepsilon_1)$$
$$l_{GHy} = -l_{GH}\cos(\alpha_1 + \beta_1 + \varepsilon_1) \quad (81)$$

$$l_{LMx} = -l_{LM}\cos(\theta_1 - \varepsilon_2 - \alpha_2 - \beta_2)$$
$$l_{LMy} = -l_{LM}\sin(\theta_1 - \varepsilon_2 - \alpha_2 - \beta_2) \quad (82)$$

$$l_{QSx} = -l_{QS}\cos(\alpha_3 - \theta_1 - \theta_2 - \beta_4 - \nu_4 - \varepsilon_4 + \rho_4)$$
$$l_{QSy} = -l_{QS}\sin(\alpha_3 - \theta_1 - \theta_2 - \beta_4 - \nu_4 - \varepsilon_4 + \rho_4) \quad (83)$$

$$l_{NQx} = -l_{NQ}\cos(\theta_1 + \theta_2 + \beta_4 + \nu_4 + \varepsilon_4 - \rho_4)$$
$$l_{NQy} = -l_{NQ}\sin(\theta_1 + \theta_2 + \beta_4 + \nu_4 + \varepsilon_4 - \rho_4) \quad (84)$$

$$l_{UQx} = -l_{UQ}\cos(\theta_1 + \theta_2 + \beta_4 + \nu_4 + \varepsilon_4 + \sigma_4)$$
$$l_{UQy} = -l_{UQ}\sin(\theta_1 + \theta_2 + \beta_4 + \nu_4 + \varepsilon_4 + \sigma_4) \quad (85)$$

where $l_{RR'x}$ and d are given by datasheets. The solution to the static equilibrium is given by:

$$\boldsymbol{x} = \boldsymbol{A}^{-1}\boldsymbol{b} \quad (86)$$

where the (29 x 1) vectors $\boldsymbol{x}$ and $\boldsymbol{b}$ are given by:

$$\boldsymbol{x} = \left(F_{Ax}, F_{Ay}, F_{Bx}, F_{By}, F_{Cx}, F_{Cy}, F_{Gx}, F_{Gy}, F_{Hx}, F_{Hy}, F_{Lx}, F_{Ly}, F_{Mx}, F_{My}, F_{Nx}, F_{Ny}, F_{QNx}, F_{QNy}, F_{QSx}, F_{QSy}, F_{QUx}, F_{QUy}, F_{Rx}, F_{Ry}, F_{R'y}, F_{Sx}, F_{Sy}, F_{Ux}, F_{Uy}\right)^T \quad (87)$$

$$\boldsymbol{b} = \big(0, m_0 g, -m_0 g l_{ACM_0x}, 0, m_1 g, m_1 g l_{ACM_1x}, 0, m_2 g, m_2 g l_{BCM_2x}, -F_{Dx}, m_3 g - F_{Dy}, -m_3 g l_{CCM_2x} - F_{Dx} l_{CDy} + F_{Dy} l_{CDx}, 0, 0, 0, 0, 0, 0, 0, 0, 0, 0, 0, 0, 0, 0, 0, 0, 0\big)^T \quad (88)$$

Concerning the tipping force F_t, it can be calculated as:

$$F_t = \left[m_0 g\left(l_{ARx} - l_{ACM_0x}\right) + m_1 g(l_{ARx} + l_{ACM_1x}) + m_2 g(l_{ARx} + l_{ABx} + l_{BCM_2x}) + m_3 g(l_{ARx} + l_{ABx} + l_{BCx} - l_{CDx})\right] \Big/ \left[(p_{Dx} + l_{ARx}) \Big/ \cos\left(\operatorname{atan}\left(\left(-p_{Dy} - d\right) \Big/ (p_{Dx} + l_{ARx})\right)\right)\right] \quad (89)$$

As the numerical scheme of the pseudocode consider increment along the x-y axis, the span of F_{Dy} is done by setting the value $F_{Dy} =$

$F_{t'}$ as upper limit, where $F_{t'}$ is obtained by F_t as:

$$F_{t'} = F_t \Big/ \cos\Big(\text{atan}\Big(\Big(-p_{Dy} - d\Big)\Big/\big(p_{Dx} + l_{ARx}\big)\Big)\Big)] \tag{90}$$

References

[1] E. G. P. I. D. G. EGIG, "11th Report of the European Gas Pipeline Incident Data Group (period 1970 – 2019)," no. December 2020, 2020.
[2] M. J. Baker, "Mechanical Damage - Final Report," 2009. doi: 10.1016/B978-0-444-99523-0.50017-9.
[3] P. Roovers, R. Bood, M. Galli, U. Marewski, M. Steiner, and M. Zaréa, "EPRG methods for assessing the tolerance and resistance of pipelines to external damage," *3R International*, vol. 2, no. Reprint, pp. 739-744,806-811, 1999.
[4] M. Allouti, C. Schmitt, G. Pluvinage, Assessment of a gouge and dent defect in a pipeline by a combined criterion, Eng. Fail. Anal. 36 (2014) 1–13, https://doi.org/10.1016/j.engfailanal.2013.10.002.
[5] P. Zhang, H. Lan, X. Dou, J. Wang, S. Zha, Review of load-bearing capacity of dented pipes under typical loads, Eng. Fail. Anal. 120 (October 2020) (2021) 105006, https://doi.org/10.1016/j.engfailanal.2020.105006.
[6] A. Rusin *et al.*, "Analysis of the Effects of Failure of a Gas Pipeline Caused by a Mechanical Damage," 2021, doi: 10.3390/en14227686.
[7] A. Cosham and P. Hopkins, "The pipeline defect assessment manual," *Proceedings of the International Pipeline Conference, IPC*, vol. B, pp. 1565–1581, 2002, doi: 10.1115/IPC2002-27067.
[8] D.C. Brooker, Experimental puncture loads for external interference of pipelines by excavator equipment, Int. J. Press. Vessel. Pip. 82 (11) (2005) 825–832, https://doi.org/10.1016/j.ijpvp.2005.07.005.
[9] I. G. N. W. Puja and N. Kollika, "Influence Of Internal Pressure To The Pipe Resistance Due To Impact Loading r l h δ ε θ α = 4 θ angle corresponding to point P P '," no. November, pp. 21–23, 2006.
[10] A.M. Gresnigt, S.A. Karamanos, K.P. Andreadakis, Lateral loading of internally pressurized steel pipes, J. Pressure Vessel Technol. Trans. ASME 129 (4) (2007) 630–638, https://doi.org/10.1115/1.2767345.
[11] A.M.N. Gresnigt, S.A. Karamanos, Response of steel tubes under concentrated lateral loads, Steel Constr. 7 (2) (2014) 133–140, https://doi.org/10.1002/stco.201410025.
[12] D.C. Brooker, Denting of pressurised pipelines under localised radial loading, Int. J. Mech. Sci. 46 (12) (2004) 1783–1805, https://doi.org/10.1016/j.ijmecsci.2004.11.004.
[13] H. Arabzadeh, M. Zeinoddini, A closed-form solution for lateral indentation of pressurized pipes resting on a flexible bed, Int. J. Mech. Sci. 75 (2013) 189–199, https://doi.org/10.1016/j.ijmecsci.2013.07.003.
[14] Y. Dou, Y. Liu, Analytical investigation and parametric study of lateral impact behavior of pressurized pipelines and influence of internal pressure, Int. J. Comput. Methods Eng. Sci. Mech. 18 (4–5) (2017) 266–276, https://doi.org/10.1080/15502287.2017.1350215.
[15] D.C. Brooker, Numerical modelling of pipeline puncture under excavator loading. Part I. Development and validation of a finite element material failure model for puncture simulation, Int. J. Press. Vessel. Pip. 80 (10) (2003) 715–725, https://doi.org/10.1016/j.ijpvp.2003.08.003.
[16] D.C. Brooker, Numerical modelling of pipeline puncture under excavator loading. Part II: Parametric study, Int. J. Press. Vessel. Pip. 80 (10) (2003) 727–735, https://doi.org/10.1016/j.ijpvp.2003.08.002.
[17] T.H. Hyde, R. Luo, A.A. Becker, Experimental validation of finite element approaches to predicting the elastic-plastic response of pipes subjected to localized indentations, J. Strain Anal. Eng. Des. 43 (7) (2008) 609–617, https://doi.org/10.1243/03093247JSA398.
[18] C. Han, S. Tan, J. Zhang, C. Zhang, Simulation investigation of dent behavior of steel pipe under external load, Eng. Fail. Anal. 90 (March) (2018) 341–354, https://doi.org/10.1016/j.engfailanal.2018.03.024.
[19] T. Xu, A. Yao, H. Jiang, Y. Li, X. Zeng, Dynamic response of buried gas pipeline under excavator loading: Experimental/numerical study, Eng. Fail. Anal. 89 (October 2017) (2018) 57–73, https://doi.org/10.1016/j.engfailanal.2018.02.026.
[20] *BS ISO 6015:2006, Earth-moving machinery-Hydraulic excavators and backhoe loaders*. 2016.
[21] P.K. Vaha, M.J. Skibniewski, Dynamic model of excavator, J. Aerosp. Eng. 6 (2) (1993) 148–158.
[22] A.J. Koivo, Kinematics of excavators (Backhoes) for transferring surface material, J. Aerosp. Eng. 7 (1) (1994) 17–32.
[23] A.J. Koivo, M. Thoma, E. Kocaoglan, J. Andrade-Cetto, Modeling and control of excavator dynamics during digging operation, J. Aerosp. Eng. 9 (1) (1996) 10–18, https://doi.org/10.1061/(asce)0893-1321(1996)9:1(10).
[24] P.H. Chang, S.-J. Lee, A straight-line motion tracking control of hydraulic excavator system, Mechatronics 12 (2002) 119–138.
[25] R. Mitrev, D. Janošević, D. Marinković, Dynamical modelling of hydraulic excavator considered as a multibody system, Tehnicki Vjesnik 24 (Sep. 2017) 327–338, https://doi.org/10.17559/TV-20151215150306.
[26] D. Janošević, J. Pavlović, V. Jovanović, G. Petrović, A numerical and experimental analysis of the dynamic stability of hydraulic excavators, Facta Univ. Ser.: Mech. Eng. 16 (2) (Aug. 2018) 157–170, https://doi.org/10.22190/FUME180404015J.
[27] R. Mitrev and D. Marinković, "Numerical study of the hydraulic excavator overturning stability during performing lifting operations," *Advances in Mechanical Engineering*, vol. 11, no. 5, May 2019, doi: 10.1177/1687814019841779.
[28] D. Vujic, O. Lazarevic, V. Batinic, Development of dynamic-mathematical model of hydraulic excavator, J. Cent. South Univ. 24 (9) (2017) 2010–2018, https://doi.org/10.1007/s11771-017-3610-x.
[29] B. Siciliano, L. Sciavicco, L. Villani, and G. Oriolo, *Robotics - Modelling, Planning and Control*. 2009.
[30] "ISO 6015, 2006: Earth-moving machinery — Hydraulic excavators and backhoe loaders — Methods of determining tool forces." International Organization for Standardization, 2006.
[31] *TM 3-34.62: Earthmoving operations*, no. June. Washington, D.C.: Headquarters, Department of the Army, 2012.
[32] "SAE J1179, 2002: Hydraulic Excavator and Backhoe Digging Forces." SAE International, 2002.
[33] D. Janosevic, R. Mitrev, B. Andjelkovic, P. Petrov, Quantitative measures for assessment of the hydraulic excavator digging efficiency, J. Zheijang Univ. Sci. A 13 (12) (2012) 926–942, https://doi.org/10.1631/jzus.A1100318.
[34] SNAM, "Caratteristiche tecniche della rete snam - rete gas." Accessed: Oct. 10, 2022. [Online]. Available: https://www.snam.it/it/trasporto/Processi_Online/ReteSnamReteGas/informazioni/rete-carat-tecniche/2_carat-tec-rete.html.
[35] Komatsu, "PC240LC/NLC-10 Excavator." Accessed: Jan. 08, 2024. [Online]. Available: https://www.komatsu.eu/it/archivio-prodotti/standard-crawler-excavators/pc240lcnlc-10.
[36] J. Lu, W. Wu, Z. Zhang, and J. Zhang, "Probability calculation of equipment impact based on reliability method," in *Proceedings of the 2014 10th International Pipeline Conference (IPC2014)*, 2014.